Available online at www.sciencedirect.com

ScienceDirect

Procedia Structural Integrity 80 (2026) 339–351

Structural Integrity Procedia

www.elsevier.com/locate/procedia

Fracture, Damage and Structural Health Monitoring

Mechanical performance of 3D printed SS 316L TPMS lattices: A computational and experimental approach

Anand K. Singh[a,c] , Thi Ngoc Diep Tran[b], Vinit V. Deshpande[b] , Stefan Dietrich[a], Volker Schulze[a] , Kamal K. Kar[c] , Romana Piat[b,*]

[a]*Institute for Applied Materials – Materials Science (IAM-WK), Karlsruhe Institute of Technology Campus South, Engelbert-Arnold-Straße 4, 76131 Karlsruhe, Germany*

[b]*Department of Mathematics and Natural Sciences, Darmstadt University of Applied Sciences, Schoefferstrasse 3, Darmstadt 64295, Germany*

[c]*Advanced Nanoengineering Materials Laboratory, Materials Science Programme, Indian Institute of Technology Kanpur, Kanpur 208016, India*

Abstract

Lightweight structures are critical in engineering applications where minimizing mass without compromising mechanical integrity is essential. This is particularly important in aerospace, automotive, and unmanned aerial vehicles, where energy absorption and controlled failure under impact are vital. Triply Periodic Minimal Surface lattices offer high structural efficiency among various geometries due to their continuous surfaces and uniform stress distribution. This study investigates the mechanical performance of 3D printed TPMS lattices made from Stainless Steel 316L (SS 316L), using diamond, gyroid, primitive, and IWP geometries. Samples with 30%, 40%, and 50% volume fractions were fabricated via Selective Laser Melting and evaluated under uniaxial compression. Finite Element Analysis was conducted in ABAQUS using the Johnson-Cook material model to simulate deformation and stress response. Compression testing was performed using a Universal Testing Machine with Digital Image Correlation, supported by X-ray Computed Tomography and Archimedes density measurements. The influence of post-processing heat treatment was also examined, which resulted in improved energy absorption but a reduction in overall stiffness. A strong correlation between simulation and experimental results confirmed the model's validity.

Keywords: TPMS lattices, 316L stainless steel, Selective Laser Melting, Finite Element Analysis, Digital Image Correlation

Corresponding author. Tel.: +49-6151-16-30030.

E-mail address: romana.piat@h-da.de

10.1016/j.prostr.2026.02.033

1. Introduction

Lightweight structures are crucial in applications demanding high performance with reduced mass, such as aerospace, automotive, and unmanned aerial vehicles (UAVs). Traditional lattice structures like BCC and FCC have been widely used to achieve such weight reduction, but they often suffer from stress concentrations and limited design flexibility (Wang et al. (2022)). To overcome these drawbacks, Triply Periodic Minimal Surface (TPMS) structures have emerged, offering smooth geometries, high surface area, and uniform stress distribution (Feng et al. (2022)). Their mathematically defined architectures allow precise control over geometry and porosity. Recent advancements in additive manufacturing (AM), particularly Selective Laser Melting (SLM), have enabled the fabrication of these complex TPMS designs with high accuracy, opening new possibilities for structural optimization in lightweight and energy-absorbing components.

The studies performed in the area of lightweight structures are mostly related to the traditional lattices such as BCC and FCC, as discussed in Flores et al. (2020). Also, SLM-fabricated 316L stainless steel lattice structures, particularly those based on a tetrakaidecahedron unit cell, are investigated to demonstrate improved compressive behaviour and energy absorption efficiency under varying laser energy densities, as validated through both experimental testing and finite element simulations (Zhong et al. (2019)). To overcome the disadvantages of traditional lattices, a new field of study emerged with the use of minimal surfaces, which have proven to provide several advantages as compared to the earlier lattices (Hsieh et al. (2021)). After the introduction of these surfaces and commonly known as TPMS a lot of work have been done in the TPMS lattice structures with polymeric materials (Maskery et al. (2018)), with very few studies involving metallic structures, for which they still lack for complete investigation of computational analysis, followed by experimental validation. The various applications of TPMS geometries in multifunctional mechanical metamaterials and the use of powder bed fusion techniques for the manufacturing of the lattices have been studied in detail by Al-Ketan and Abu Al-Rub (2019). Some researchers have used functionally graded stainless steel lattices with TPMS geometries, but the computational simulations are not presented (Ravichander et al. (2022)). In another study by Tran and Piat (2026), the effect of cell geometry and volume fractions on the damage behaviour of sheet TPMS lattices was studied.

This study focuses on the design and SLM-based fabrication of TPMS lattice structures with varying geometries and volume fractions. The printed lattices are characterized using X-ray Computed Tomography (CT) scanning, compression testing, and porosity evaluation. Post-processing effects via heat treatment are also examined. Finite Element Analysis (FEA) is used to simulate mechanical behavior, and results are compared with experiments to validate deformation patterns and assess structural performance.

2. Materials and Methodology

The samples were fabricated using 316L stainless steel powder supplied by m4p material solutions GmbH, Germany, and the chemical composition of the as-received powder is provided in Table 1. The particle size range of the powder was from 15 to 45 micrometers with close to spherical shapes.

Table 1. Chemical Composition of SS 316 in weight%.

C	Si	Mn	Ni	Cr	Mo	Fe
0.02	0.7	1.1	11.1	17.0	2.3	67.78

3. Computational modelling and design methodologies

3.1 TPMS model generation

The TPMS structures used in this study were generated using MSLattice, a software tool developed by New York University Abu Dhabi (Al-Ketan and Abu Al-Rub, (2021)). This tool features a MATLAB (MathWorks (2022)) based GUI where the Mathematical equations of the geometries are input into the GUI, which then processes them to create and plot the corresponding iso-surfaces, which can be either sheet or solid. This study focuses exclusively on uniform TPMS lattices with constant geometry and volume fraction throughout.

The important parameters to consider while modelling the TPMS geometries are relative density, unit cell size, sample dimensions (length, width, and height), and mesh density points. The unit cell defines the smallest repeating structure, which, when replicated along different directions, forms the periodic lattice. In a study by Jones et al. (2022), it was found that the number of lattices has a direct impact on the effective elastic stiffness, and hence, to reduce this to a minimum, a size of 3x3 lattices was chosen for the current study. The relative density determines the solid phase volume fraction in the lattice and is defined concerning the total volume of the enclosing cuboid formed by the sample's length, width, and height. Mesh density per unit cell refers to the number of grid points defined within a single unit cell, which was found to be optimum with reduced computational cost and time when chosen as 30 by Jones et al. (2022). The process of creating the geometries for experimental and computational purposes is summarised in the flowchart presented in Fig. 1. Finally, the selected TPMS models are presented in Fig. 2. (a) and the dimensions of the unit cell and also of the 3x3 lattice in Fig. 2. (b).

The cross-sectional area variation along the height of the TPMS structures under loading is illustrated in Fig. 2. (c). The Primitive design shows a sharp gradient of change in cross-sectional area, with narrow neck regions near the edges, indicating localised failure under compression. In contrast, the Gyroid and Diamond exhibit more uniform area profiles, promoting better load distribution, mechanical stability, and progressive deformation. The IWP structure shows intermediate behaviour with smoother transitions. These geometric differences help explain the distinct deformation responses observed among the designs, aligning with findings by Maskery et al. (2018).

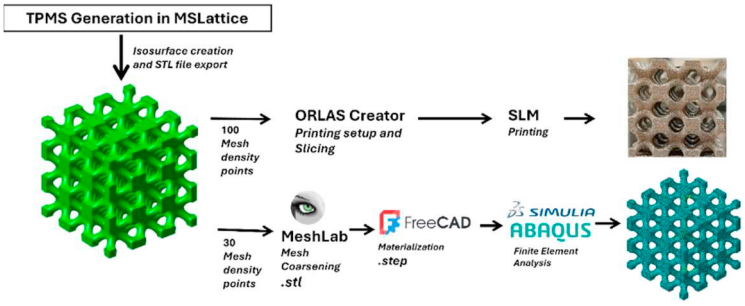

Fig. 1. Workflow to create the geometries for experimental and computational purposes.

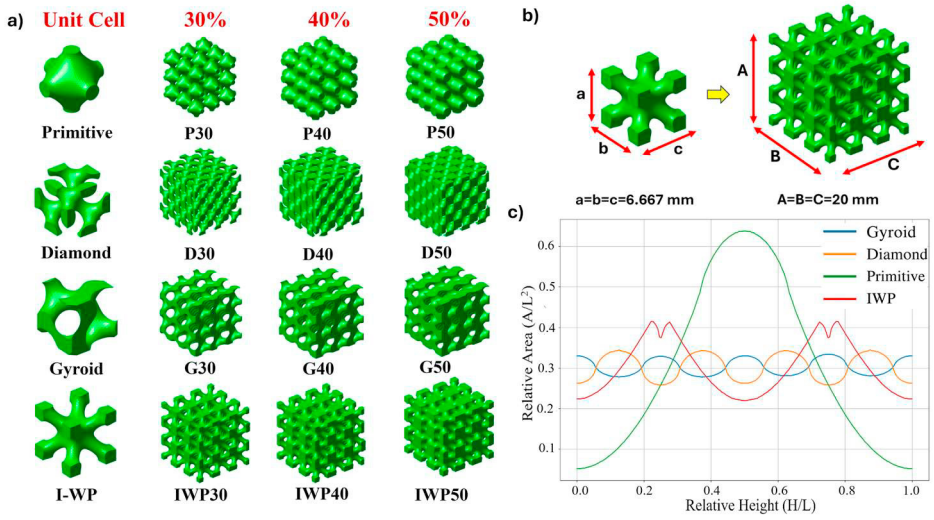

Fig. 2. (a) TPMS models studied in this work; (b) dimensions of unit cell and full lattice; (c) normalized cross section area variation along all axes.

3.2 Finite Element Analysis

The FEA to simulate TPMS lattice structures in ABAQUS/Explicit (Dassault Systèmes (Simulia), (2023)), the as-designed STL geometries generated using MSLattice were first converted into a solid-compatible format. Since STL files cannot be directly used for solid meshing, a two-step process was adopted as shown in Fig. 1. Initially, the STL meshes were coarsened in MeshLab (MeshLab, (2023)) to reduce computational cost while preserving essential geometry. The simplified mesh was then imported into FreeCAD (FreeCAD, (2023)) and converted into STEP format, enabling solid modelling in ABAQUS. Similar workflows have been reported for TPMS structures in previous studies Tran and Piat (2026). Initial simulations were performed on single-unit-cell models for each TPMS type. This approach facilitated rapid troubleshooting before transitioning to full-scale lattice simulations, ensuring both accuracy and computational efficiency.

3.2.1 Material Model

To accurately capture the elastic-plastic response of metallic TPMS lattices under quasi-static compression, the Johnson–Cook (JC) constitutive model was adopted. This model is well-suited for large deformations and strain-rate-sensitive plasticity, making it ideal for simulating the nonlinear mechanical behaviour of metals such as 316L stainless steel (Yang et al. (2017a)). The JC model describes the plastic flow stress given in equation (1) as a function of plastic strain and strain rate:

$$\sigma_{\mathrm{eq}} = \left[A + B\varepsilon_p^n\right]\left[1 + C \cdot \ln\left(\frac{\dot{\varepsilon_p}}{\dot{\varepsilon_0}}\right)\right]\left[1 - \left(\frac{T - T_{\mathrm{room}}}{T_{\mathrm{melt}} - T_{\mathrm{room}}}\right)^m\right]. \tag{1}$$

In the current work, the thermal effects were excluded from the model since the loading conditions were quasi-static and isothermal, meaning the temperature rise during deformation was negligible. Thus, the thermal term in the JC equation was omitted, simplifying the model while retaining its ability to capture plastic and strain rate behaviour:

$$\sigma_{\mathrm{eq}} = \left[A + B\varepsilon_p^n\right]\left[1 + C \cdot \ln\left(\frac{\dot{\varepsilon_p}}{\dot{\varepsilon_0}}\right)\right]. \tag{2}$$

Table 2. JC parameters used in this study.

Parameter	Value	Parameter	Value
Initial yield strength (A)	380 MPa	reference strain rate $\dot{\varepsilon_0}$	0.001
Hardening modulus (B)	825 MPa	Elastic Modulus (E)	200 GPa
Strain hardening exponent (n)	0.726	Poisson's Ratio	0.33
Strain rate sensitivity coefficient (C)	0.115	Density	7.85×10^{-09} mm^3/tonne

The JC parameters used in the simulations were taken from a study in which additively manufactured samples by SLM with 316L stainless steel were tested under compression (Yang et al., (2017b)). Table 2 shows the material properties and the JC parameters used for this study. This allowed for accurate prediction of the material's deformation behaviour within the finite element framework used for analysing the TPMS lattice structures. The damage parameters were not considered, as previous studies by Qiu et al. (2024) have shown accurate results for elastic-plastic deformation without their consideration.

3.2.2 Interaction

Contact interactions were modelled using the general contact algorithm in Abaqus/Explicit, enabling automatic detection of surface interactions, including self-contact, critical for highly deformable TPMS structures under compression. Normal behaviour was defined as hard contact to prevent penetration, while tangential behaviour employed a penalty friction formulation with a coefficient of 0.3 at the lattice–plate interfaces. This setup ensured realistic surface interaction and sliding resistance during large deformations, contributing to accurate mechanical response prediction.

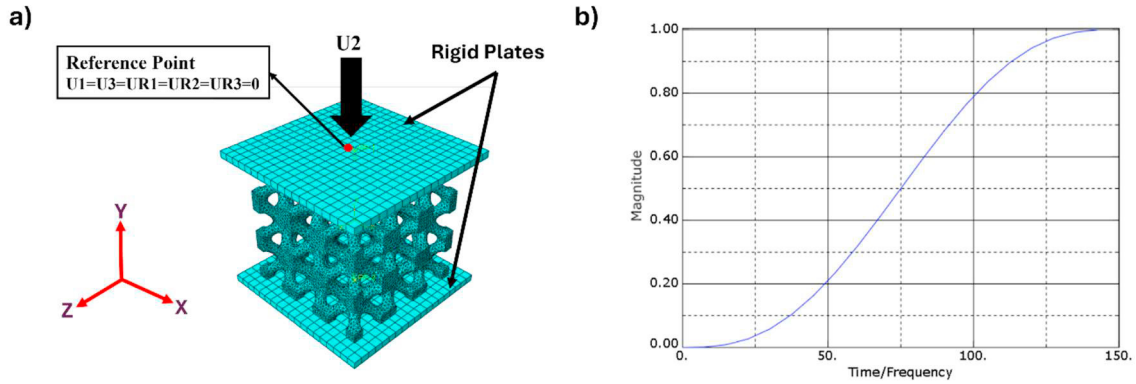

Fig. 3. (a) boundary conditions; (b) amplitude vs time plot.

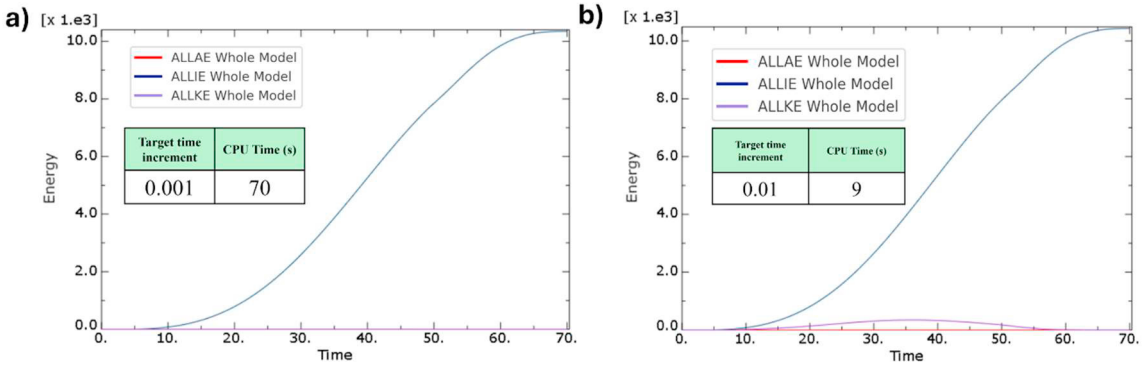

Fig. 4. Mass scaling with target time increment of: (a) 0.001 low KE; (b) 0.01 higher KE.

3.2.3 Boundary conditions

The lattice structures were compressed along the vertical axis under displacement-controlled loading. The bottom rigid plate was fully fixed using an encastre boundary condition, while a vertical displacement of approximately 9 mm was applied to the top plate, with all other degrees of freedom restricted. The lattice remained unconstrained and interacted with the plates through surface-to-surface contact, allowing natural deformation without artificial stiffening. This setup reflects the experimental conditions where densification typically initiated between 7 mm and 9 mm of top surface displacement. Fig. 3. (a) illustrates the applied boundary conditions.

3.2.4 Step definition

In Abaqus/Explicit, achieving quasi-static behaviour requires careful selection of step time and amplitude settings to control strain rate effects. A smooth step amplitude was used to gradually apply displacement, reducing artificial dynamic responses such as oscillations or inertial forces Fig. 3. (b) A step time of 150 seconds provided a close match to the experimental compression duration (~500 s) while maintaining numerical stability. Shorter durations introduced noticeable strain rate sensitivity in the force–displacement response. To further improve computational efficiency without compromising accuracy, mass scaling was applied under the step definition, as detailed in the next sections.

3.2.5 Mass Scaling

To enhance computational efficiency in explicit simulations without compromising accuracy, mass scaling was employed. This technique artificially increases material density, allowing larger stable time increments while preserving quasi-static behaviour. A semi-automatic approach was adopted by specifying a target minimum time

increment, enabling Abaqus to adjust element masses accordingly. This method effectively minimized the influence of small elements on time step size and reduced overall run time. Quasi-static conditions were verified by monitoring the energy balance throughout the simulation. Specifically, the kinetic energy (KE) was ensured to remain significantly lower than the internal energy (IE) and total energy (ALLKE), indicating minimal inertial effects.

A parametric study was conducted on the IWP unit cell to determine an optimal target time increment. Without mass scaling, the stable increment was on the order of 10^{-9} s, resulting in a simulation time of approximately 16 hours. Introducing mass scaling with a target time increment of 0.0001 s reduced the simulation time to ~1843 seconds with negligible KE influence. Further increasing the target increment to 0.001 s shortened the runtime to 70 seconds, as shown in Fig. 4. (a), while still maintaining low KE levels. However, a value of 0.01 s introduced noticeable inertial effects, as KE approached peak values before dropping, as shown in Fig. 4. (b). Based on this analysis, 0.001 s was selected as the optimal value, balancing accuracy and computational cost.

3.2.6 Meshing strategy and Convergence

Due to the complex curvature of TPMS structures, unstructured tetrahedral meshing was employed. A uniform global seed size was applied across all geometries, constrained by the surface resolution of the imported STEP files. Voxel-based hexahedral meshing, though common in literature (Feng et al., (2022)), was avoided to better capture thin features and junctions.

Convergence was assessed by comparing force–displacement curves from simulations using varying global seed sizes and element types (C3D4 and C3D10M), as shown in Fig. 5. (a) and (b). The method involved checking for overlapping curves under identical boundary conditions. A global seed size of 0.5 mm with C3D10M elements showed mesh-independent results, with negligible variation below this resolution, confirming numerical convergence.

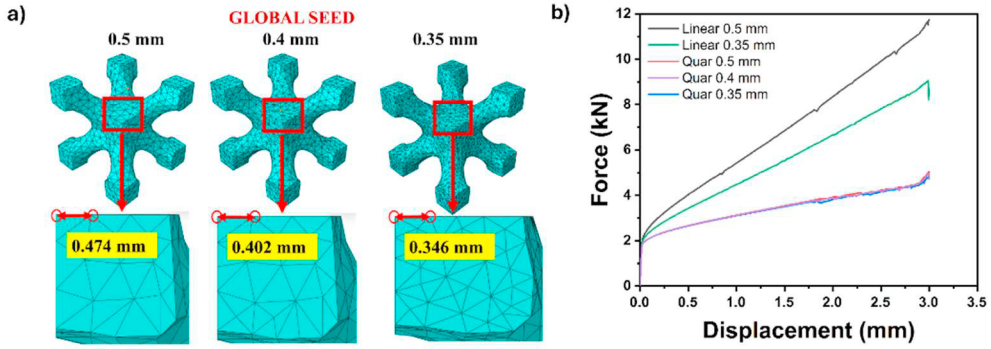

Fig. 5. (a) meshing with different global seed values; (b) mesh sensitivity plot.

4. Experimental setup

4.1 Fabrication

The samples were fabricated using the ORLAS CREATOR® SLM printer. Table 3 gives the SLM process parameters.

Table 3. Processing Parameters of SLM (Szatkiewicz et al., (2022)).

Laser Power	Laser Speed	Layer Thickness	Printing Environment
123 W	1000 mm/s	25 µm	Argon

4.2 Characterization

An X-ray CT scan was employed as a non-destructive testing method to evaluate internal defects and assess geometric fidelity. Additionally, to estimate the overall porosity in the printed samples, density measurements were

performed using the Archimedes principle with a METTLER TOLEDO® balance having a sensitivity of 0.1 mg. For mechanical characterization, compression tests were conducted using a UTM integrated with a digital image correlation (DIC) system, as shown in Fig. 6. DIC enabled full-field strain measurement by capturing the displacement of a speckle pattern applied to the sample surface. To ensure accurate strain tracking, the samples were carefully positioned within the field of view of the DIC cameras using a custom additively manufactured fixture, which eliminated misalignment and ensured repeatability across tests.

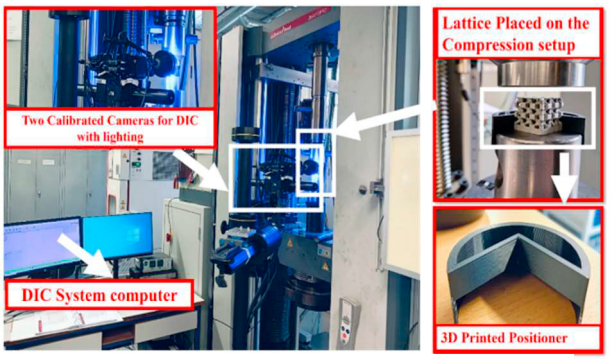

Fig. 6. UTM-DIC compression setup.

5. Results and Discussion

5.1 Porosity analysis

The printed samples, shown in Fig. 7. (a), were machined to remove the support structures, followed by ultrasonic cleaning to eliminate any residual powder. The theoretical density of the alloy was calculated using the rule of mixtures, considering the densities and weight percentages of each alloying element. As the composition was provided in weight percent (wt.%), a harmonic mean approach was used to estimate the bulk density as a volumetric property, which was calculated to be 7.75 g/cm³. This value served as the reference for porosity estimation. Among all structures, the primitive lattice exhibited the lowest porosity, and the percentage porosity for each sample is plotted in Fig. 7. (b). A rectangular sample with equivalent volume to the 50% TPMS structures showed a porosity of just 0.7%, indicating that higher surface complexity in TPMS geometries is associated with increased porosity.

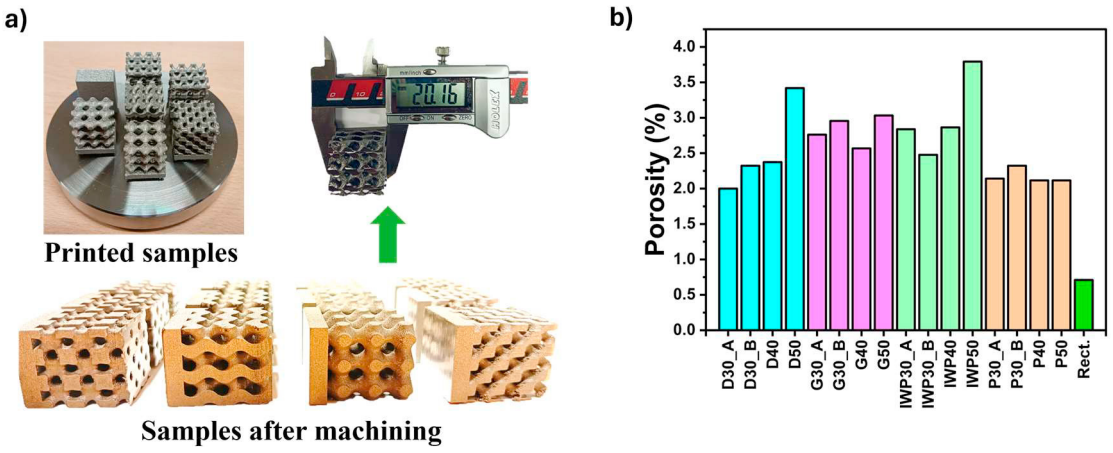

Fig. 7. (a) representation of printed samples; (b) porosity analysis.

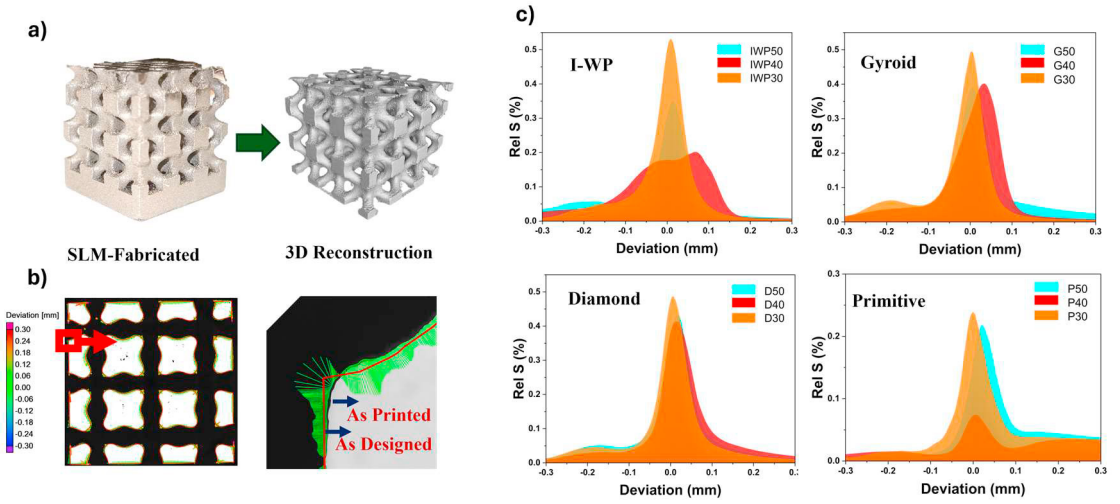

Fig. 8. (a) CT reconstruction of IWP 30; (b) designed vs printed comparison; (c) nominal to actual deviations for all samples.

5.2 CT Scan results

The CT reconstruction of the IWP30 lattice is shown in Fig. 8. (a) Due to the high density of stainless steel, the CT scans exhibited low contrast and noise, limiting porosity accuracy; hence, the CT-derived porosity was higher than the Archimedes value. For the dimensional accuracy, it was seen that the deviations were mostly within ±0.1 mm, which can be seen in Fig. 8. (b), where the designed vs printed geometry is compared. In Fig. 8. (c), the histogram plot for the deviation vs the relative surface area plot is shown. A more reliable approach involves printing a small sample, calibrating porosity with the Archimedes method, and then applying the optimized parameters for final prints.

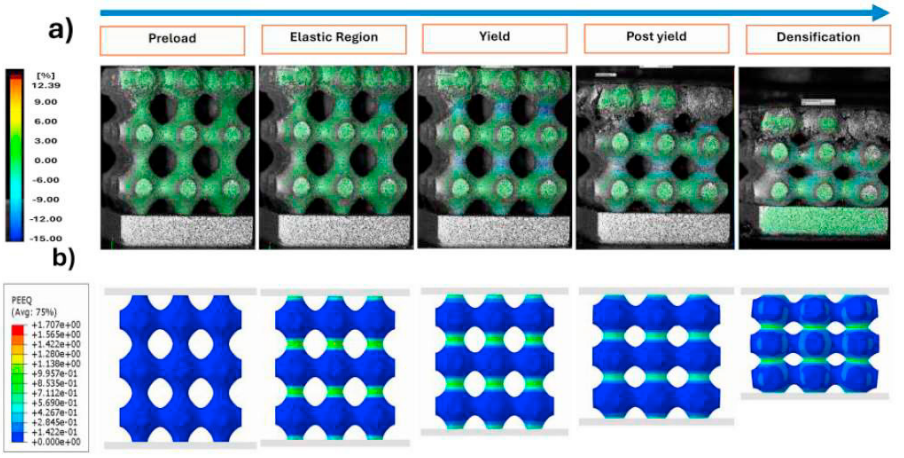

Fig. 9. Compression stages for the P40 as observed in (a) UTM-DIC; (b) PEEQ in Abaqus (FEA).

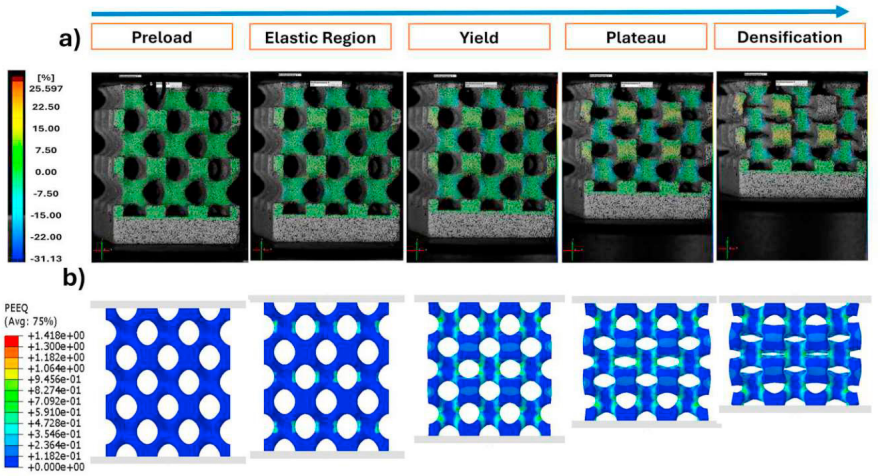

Fig. 10. Compression stages for the IWP30 as observed in (a) UTM-DIC; (b) PEEQ in Abaqus (FEA).

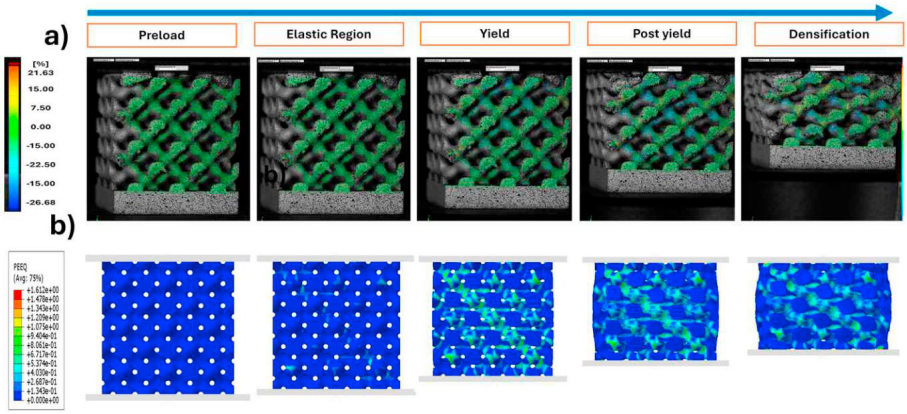

Fig. 11. Compression stages for the D30 as observed in (a) UTM-DIC; (b) PEEQ in Abaqus (FEA).

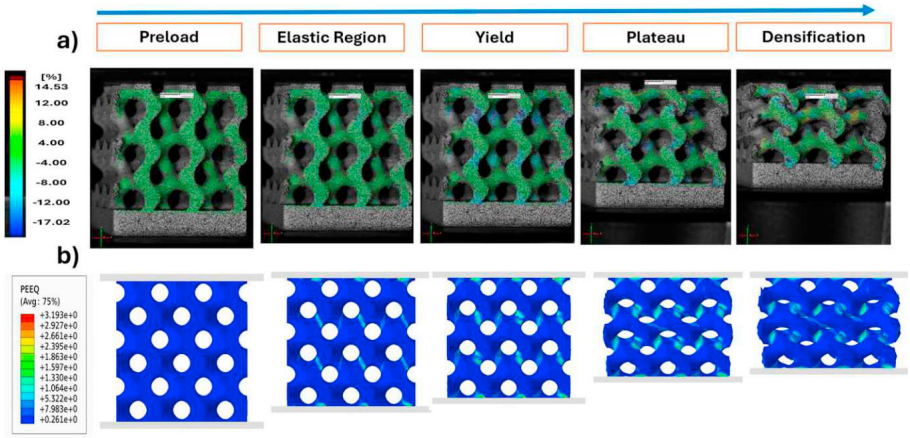

Fig. 12. Compression stages for the G30 as observed in (a) UTM-DIC; (b) PEEQ in Abaqus (FEA).

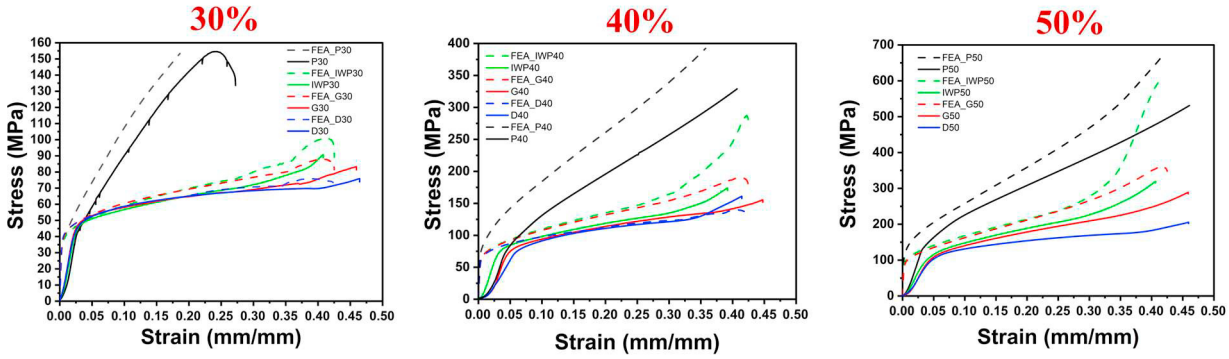

Fig. 13. The experimental and FEA stress strain plots for different volume fractions.

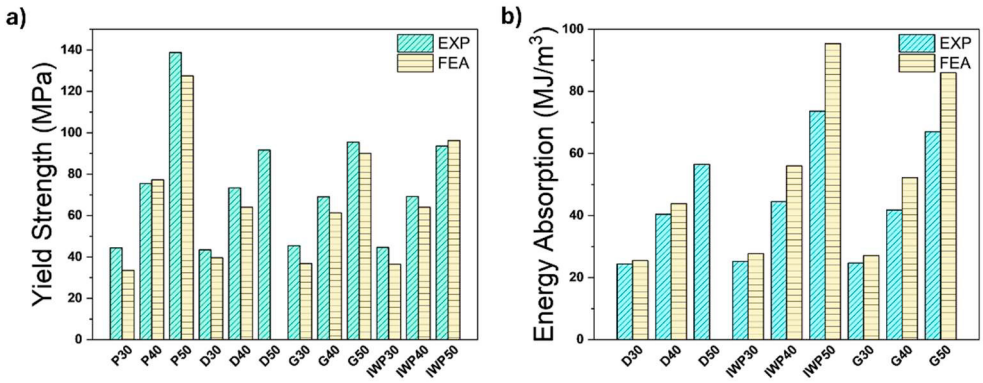

Fig. 14. EXP vs FEA results for (a) yield strength; (b) energy absorption.

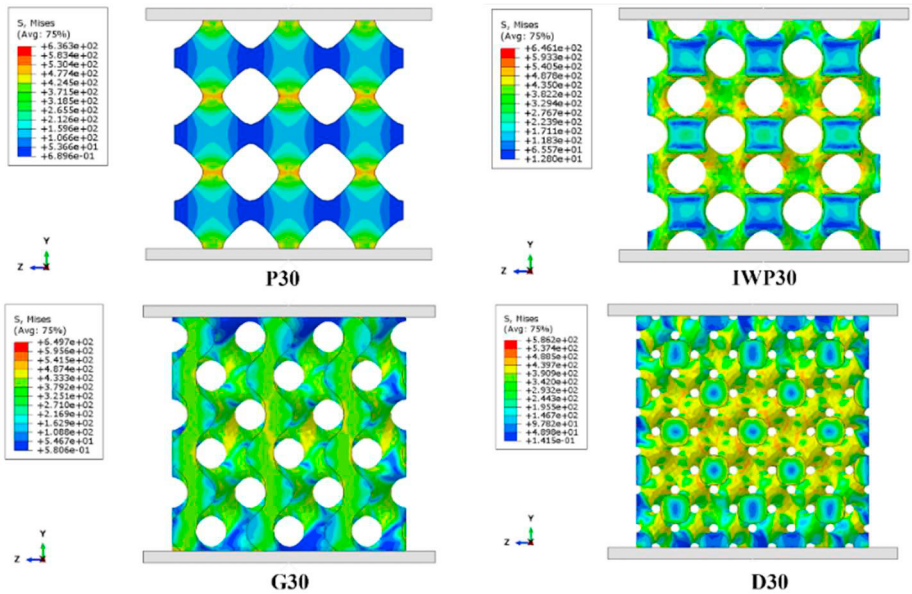

Fig. 15. Von Misses strain distribution shown for 30% and similar for 40% and 50%.

5.3 Compression Behaviour and Failure Mechanisms

The deformation behaviour is shown in Fig. 9, Fig. 10, Fig. 11, and Fig. 12 for P40, IWP30, D30, and G30, respectively. The primitive structures exhibited a stretching-dominated deformation pattern, with the P30 lattice showing early failure initiated by asymmetric buckling and collapse on one side. In contrast, the P40 and P50 lattices experienced more symmetric surface buckling and localized failure in the neck regions, where the reduced cross-sectional area induced stress concentration. On the other hand, the gyroid, diamond, and IWP lattices displayed bending-dominated behaviour, characterized by progressive collapse and the formation of shear bands along thinner struts. These shear localized regions correspond to zones of high bending stress and mark the primary failure mechanism in these geometries.

5.3.1 Stress-strain behavior

The combined stress–strain plot, Fig. 13, shows strong agreement between FEA and experimental results, especially in the plastic and densification regimes. The comparative overview of yield strength is shown in Fig. 14. (a), and strain energy absorption is shown in Fig. 14. (b) for all TPMS geometries and volume fractions. For yield strength, FEA predictions align well with experimental values, with errors largely limited to within ±13%. The most notable deviation is observed in the primitive structure at 30%, where yield strength is underestimated due to stress localization in narrow neck regions not fully resolved in the mesh. Similarly, for strain energy absorption, the error remained within ±10% in most cases, except for a few instances, such as the IWP and gyroid structures at 50%, where deviations reached up to ~30%, likely due to increased sensitivity to manufacturing-induced defects at higher densities. The corresponding Von Mises stress distribution during the elastic regime is also shown in Fig. 15, highlighting differences in load transfer mechanisms. The primitive structure exhibits concentrated stresses at the neck regions, confirming a stretching-dominated response. In contrast, the diamond, gyroid, and IWP structures show more uniform stress fields, indicative of bending-dominated deformation with enhanced energy absorption but lower initial stiffness. Overall, the numerical model demonstrates reliable predictive capability for the mechanical performance of TPMS structures. Incorporating tensile-derived input properties and defect-informed modelling approaches could further reduce the remaining discrepancies.

5.2 Heat treatment effect

The compression response of the heat-treated (HT) primitive structure exhibited surface delamination near the densification region, as shown in Fig. 16. (a). In comparison, the non-heat-treated (N-HT) lattice maintained structural cohesion under load. CT scans of the heat-treated sample Fig. 16. (b) revealed increased porosity concentrated along the outer surfaces, compromising surface integrity and contributing to early delamination during compression. The stress-strain curve is shown in Fig. 16. (c), and it can be concluded from this that the nature of the curves remains almost the same for both the. Mechanical property comparisons summarized in Table 4 indicate that heat treatment led to a reduction in stiffness, reflecting the structural weakening caused by elevated porosity. However, strain energy absorption and yield strength remained largely unaffected, suggesting that energy dissipation capability was retained despite the reduction in stiffness, hence, this can be used in applications where low stiffness, but high energy absorption is required.

Table 4. Mechanical properties of the heat-treated sample.

Structure	**Effective Elastic Modulus (GPa)**			**Yield Strength (MPa)**			**Energy absorption (MJ/m^3)**		
	N-HT	HT	%Change	N-HT	HT	%Change	N-HT	HT	%Change
Primitive	2.27	1.33	-41.4	44.43	39.81	-10.40	-	-	-
Gyroid	2.19	1.44	-34.3	45.36	42.89	-5.45	21.02	19.60	-6.76
Diamond	2.34	1.75	-25.2	43.43	41.25	-5.02	20.95	20.49	-2.20
IWP	2.17	1.33	-38.7	44.59	39.24	-12.00	21.13	21.63	2.37

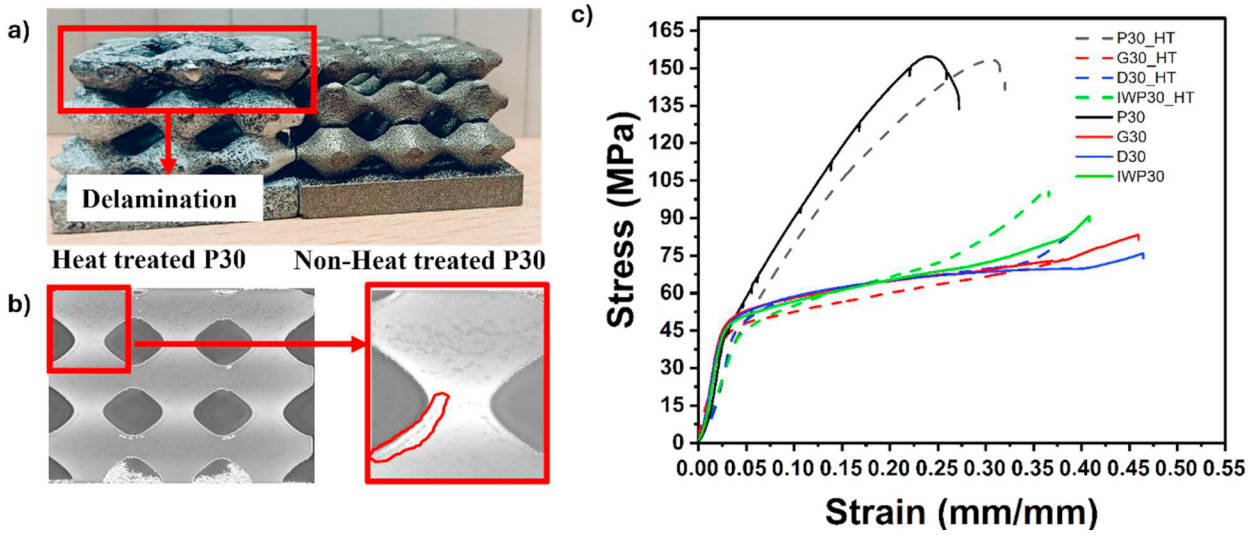

Fig. 16. (a) delamination of the P30 heat treated lattice; (b) the CT scan shows the porous contour following the outer surface; (c) stress strain plot for N-HT and HT.

6. Conclusions

The mechanical behaviour of TPMS lattice structures under compressive loading was systematically investigated through both experimental and computational approaches. The influence of geometry, volume fraction, and post-processing treatment on deformation and failure mechanisms was assessed using a combination of CT-based porosity analysis, quasi-static compression testing, and finite element simulations.

Based on the observations and results obtained, the following conclusions can be drawn:

- TPMS lattice structures were fabricated via SLM with high geometric precision; CT scans showed dimensional deviations typically within ±0.1 mm from the designed models. Porosity measured using the Archimedes method averaged around 2.5% and was more consistent than CT-based values, which were influenced by noise and limited contrast. Higher surface area structures exhibited slightly increased porosity due to surface-connected defects.
- Compression tests revealed geometry-dependent deformation modes. Primitive lattices showed stretching-dominated behavior without a defined plateau, whereas gyroid, diamond, and IWP lattices exhibited bending-dominated deformation with clear plateau and densification phases. Increasing volume fraction enhanced structural stiffness and delayed failure. P30 structures failed at lower strains, while P40 and P50 reached densification with a stiffer response but limited plateau behavior.
- FEA simulations were implemented with mass scaling, significantly reducing computational time without compromising accuracy. The results showed strong agreement with experimental data in the plastic and densification regimes, while deviations in the elastic region were attributed to idealized boundary conditions and material assumptions. Von Mises stress analysis further revealed stress concentrations at narrow necks and sharp features, aligning with observed failure zones in compression testing.
- Heat-treated lattices had decreased stiffness in the elastic region suggesting that these can be used in applications where the energy absorption need is high with lower stiffness requirements. The primitive lattice exhibited delamination near the densification region, attributed to outer surface porosity. This highlights the need for optimized processing conditions to reduce such defects.

Acknowledgements

The authors would like to thank the Institute for Applied Materials at the Karlsruhe Institute of Technology (IAM-KIT) for providing the experimental infrastructure and technical support essential to this research. Financial support

from the German Academic Exchange Service (DAAD) under the KOSPIE program is gratefully acknowledged. The authors also appreciate the collaboration and academic support from the Indian Institute of Technology Kanpur and the University of Applied Sciences Darmstadt.

References

Al-Ketan, O., Abu Al-Rub, R.K., 2021. MSLattice: A free software for generating uniform and graded lattices based on triply periodic minimal surfaces. Mat Design & Process Comms. 3.

Al-Ketan, O., Abu Al-Rub, R.K., 2019. Multifunctional Mechanical Metamaterials Based on Triply Periodic Minimal Surface Lattices. Adv Eng Mater 21, 1900524.

Dassault Systèmes (Simulia), 2023. ABAQUS. Dassault Systèmes (Simulia). https://www.3ds.com/products-services/simulia/products/abaqus/.

Feng, J., Fu, J., Yao, X., He, Y., 2022. Triply periodic minimal surface (TPMS) porous structures: from multi-scale design, precise additive manufacturing to multidisciplinary applications. Int. J. Extrem. Manuf. 4, 022001.

Flores, I., Kretzschmar, N., Azman, A.H., Chekurov, S., Pedersen, D.B., Chaudhuri, A., 2020. Implications of lattice structures on economics and productivity of metal powder bed fusion. Additive Manufacturing 31, 100947.

FreeCAD (Version 0.21.2). https ://www.freecad.org/

Hsieh, M.-T., Begley, M.R., Valdevit, L., 2021. Architected implant designs for long bones: Advantages of minimal surface-based topologies. Materials & Design 207, 109838.

Jones, A., Leary, M., Bateman, S., Easton, M., 2022. Parametric design and evaluation of TPMS-like cellular solids. Materials & Design 221, 110908.

J. Feng, J. Fu, X. Yao, Y. He, Triply periodic minimal surface (TPMS) porous structures: from multi-scale design, precise additive manufacturing to multidisciplinary applications, Int. J. Extreme Manuf. 4 (2022) 022001.

Maskery, I., Sturm, L., Aremu, A.O., Panesar, A., Williams, C.B., Tuck, C.J., Wildman, R.D., Ashcroft, I.A., Hague, R.J.M., 2018. Insights into the mechanical properties of several triply periodic minimal surface lattice structures made by polymer additive manufacturing. Polymer 152, 62–71.

MathWorks, 2023. Version R2023b. Natick, Massachusetts: https://de.mathworks.com/products/new_products-/release2023b.html

MeshLab (Version 2023.12). https://www.meshlab.net/

Qiu, N., Wan, Y., Shen, Y., Fang, J., 2024. Experimental and numerical studies on mechanical properties of TPMS structures. International Journal of Mechanical Sciences 261, 108657.

Ravichander, B.B., Jagdale, S.H., Kumar, G., 2022. Surface Morphology, Compressive Behavior, and Energy Absorption of Graded Triply Periodic Minimal Surface 316L Steel Cellular Structures Fabricated by Laser Powder Bed Fusion. Materials 15, 8294.

Szatkiewicz, T., Laskowska, D., Bałasz, B., Mitura, K., 2022. The Influence of the Structure Parameters on the Mechanical Properties of Cylindrically Mapped Gyroid TPMS Fabricated by Selective Laser Melting with 316L Stainless Steel Powder. Materials 15, 4352.

Tran, T.N.D., Piat, R., 2026. Correlation between the structural geometry and damage localization of Triply periodic minimal surface-based ceramic unit cells, Procedia Structural Integrity THIS ISSUE (2026)

Wang, M., Zhang, J., Wang, W., 2022. Compression and Deformation Behaviors of Hierarchical Circular-Cell Lattice Structure with Enhanced Mechanical Properties and Energy Absorption Capacity. Aerospace 9, 786.

Yang, Z., Yu, Y., Wei, Y., Huang, C., 2017b. Crushing behavior of a thin-walled circular tube with internal gradient grooves fabricated by SLM 3D printing. Thin-Walled Structures 111, 1–8.

Zhong, T., He, K., Li, H., Yang, L., 2019. Mechanical properties of lightweight 316L stainless steel lattice structures fabricated by selective laser melting. Materials & Design 181, 108076.